Journal of Physics and Chemistry of Solids 148 (2021) 109670

Contents lists available at ScienceDirect

Journal of Physics and Chemistry of Solids

journal homepage: http://www.elsevier.com/locate/jpcs

Experimental and DFT study of $BaLaCuS_3$: Direct band gap semiconductor

A.S. Oreshonkov [a,b,*], N.O. Azarapin [c], N.P. Shestakov [a], S.V. Adichtchev [d]

[a] Laboratory of Molecular Spectroscopy, Kirensky Institute of Physics, Federal Research Center KSC SB RAS, Krasnoyarsk, 660036, Russia
[b] School of Engineering and Construction, Siberian Federal University, Krasnoyarsk, 660041, Russia
[c] Institute of Chemistry, Tyumen State University, Tyumen, 625003, Russia
[d] Institute of Automation and Electrometry, Russian Academy of Sciences, Novosibirsk 630090, Russia

ARTICLE INFO

Keywords:
Sulphidation
Semiconductor
Direct band gap
Wide band gap
Solar cell

ABSTRACT

$BaLaCuS_3$ powder was prepared by sulphidation method. The shape of powder particles is irregular and place in the range of 10–100 μm. The electronic, elastic and vibrational properties were evaluated with the use of DFT method. According to the electronic band structure calculation the $BaLaCuS_3$ is a direct wide band gap semiconductor with $E^d_g = 2.0$ eV while the energy of indirect transition is equal to 2.2. eV and it indicates that the $BaLaCuS_3$ is a promising material for efficient underwater solar cells. Calculated compressibility of $BaLaCuS_3$ is found to be identical to germanium and zinc blende modification of zunc sulfide.

1. Introduction

The wide band gap (WBG) semiconductors are materials with band gap value above 2.0 eV [1]. At present, developments in semiconductor materials stimulated an interest in WBG and wide band gap devices can be expected to comprise over 12% of the power electronics market by 2025 [2]. The optoelectronic applications of WBG are associated with production of green, blue-ultraviolet and white light-emitting devices. The widely used materials in this field are GaN and ZnO WBG semiconductors with band gap values (E_g) equal to 3.4 and 3.3 eV correspondingly [3]. In 1972, Fujishima and Honda reported about photoelectrochemical splitting of water using a WBG TiO_2 anode (E_g = 3.0–3.2 eV [4]) and a Pt electrode [5].

The underwater vehicles and devices are strongly limited by the lack of long-lasting power sources. Recently, it has been shown that WBG semiconductors can be used as underwater solar cell media and the optimum band gap value is found to be 2.1 eV [6]. As for the silicon, this material is abundant in nature and the band gap value of cubic silicon is a bit lower than theoretical value of Shockley–Queisser limit (1.34eV) [7–9] that have been calculated for the earth's surface but not under the sea.

The $BaLaCuS_3$ semiconductor needle-like crystals was synthesized for the first time by Christuk [10]. This material crystallizes in the centrosymmetric *Pnma* space group. The unit cell parameters of orthorhombic BLCS ($BaLaCuS_3$) were determined at $T = 115$ K as $a = 11.316$ (2) Å, $b = 4.236$ (1) Å, $c = 11.724$ (2) Å. The optical band gap was defined as 2.00 (2) eV from diffuse reflective UV–visible spectra [10]. The variation of measured optical band gap values in Ba*Ln*CuS_3 (Ln = rare-earth ions of Y) presented in Table S1 of Supporting Information.

The present work is aimed to the preparation of $BaLaCuS_3$ powder for a relative short time in comparison with Crhistuk's work [10] and examination of it's thermal, electronical, elastic and vibrational properties.

2. Materials and methods

2.1. Synthesis

The $BaLaCuS_3$ powder was obtained by sulfidation of the oxide mixture after co-nitration of the starting components followed by temperature decomposition. The following high purity reagents were used as the starting materials: Cu (99,9%, SZB Tsvetmet, Russia), $BaCO_3$ (99,99%, ultrapure, KAI YONG, China), La_2O_3 (99,99%, ultrapure, TDM-96 Ltd. Russia) and concentrated nitric acid solution ($C(HNO_3)$ = 0.0146 mol/m^3, ultrapure, Vekton Ltd., Russia). Ammonium thiocyanate NH_4SCN (98%, VektonLtd., Russia).

The first step in synthesis of $BaLaCuS_3$ by sulphidation method is the preparation of the initial oxide mixture. Initial reagents were taken at the stoichiometric molar ratio $2Cu:La_2O_3:2BaCO_3$ (Cu – 0.8194 g, La_2O_3 – 2.1005 g, $BaCO_3$ – 2.5444 g). A 500 ml heat-resistant chemical beaker was used to dissolve the starting components. The mix of components was dissolved in excess concentrated nitric acid (HNO_3). For better

* Corresponding author. Laboratory of Molecular Spectroscopy, Kirensky Institute of Physics, Federal Research Center KSC SB RAS, Krasnoyarsk, 660036, Russia.
E-mail address: oreshonkov@iph.krasn.ru (A.S. Oreshonkov).

https://doi.org/10.1016/j.jpcs.2020.109670
Received 6 May 2020; Received in revised form 14 July 2020; Accepted 16 July 2020
Available online 27 July 2020

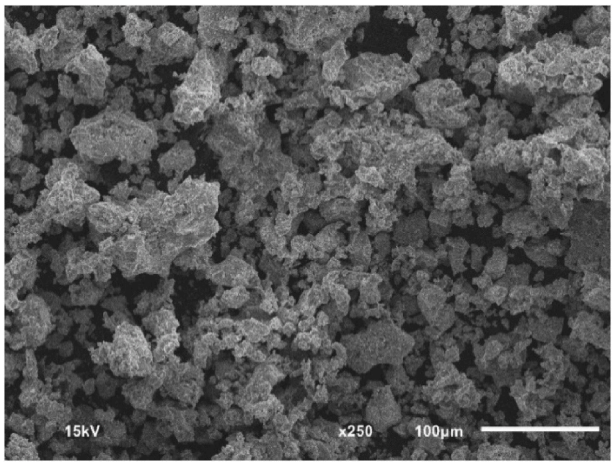

Fig. 1. Scanning electron microscopy micrograph of $BaLaCuS_3$ powder.

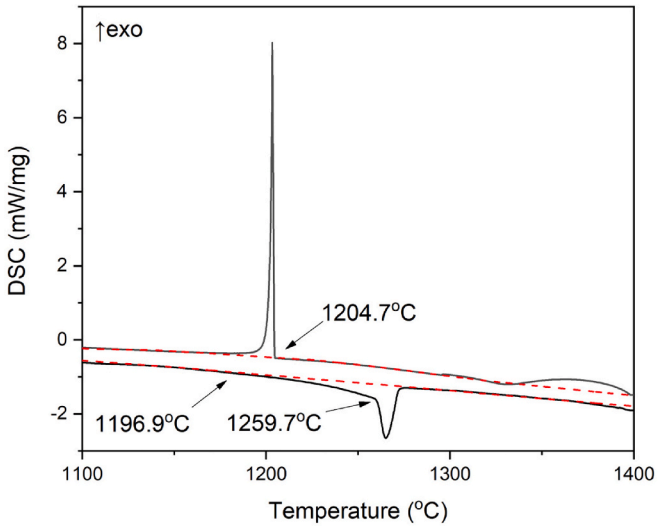

Fig. 2. DTA curves recorded for powder sample of BaLaCuS3. The baselines are shown in red color.

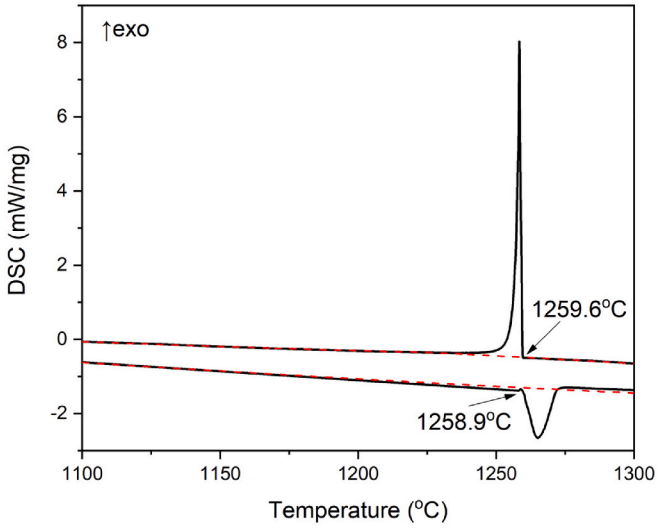

Fig. 3. DTA of second curves recorded for BaLaCuS3. The baselines are shown in red color.

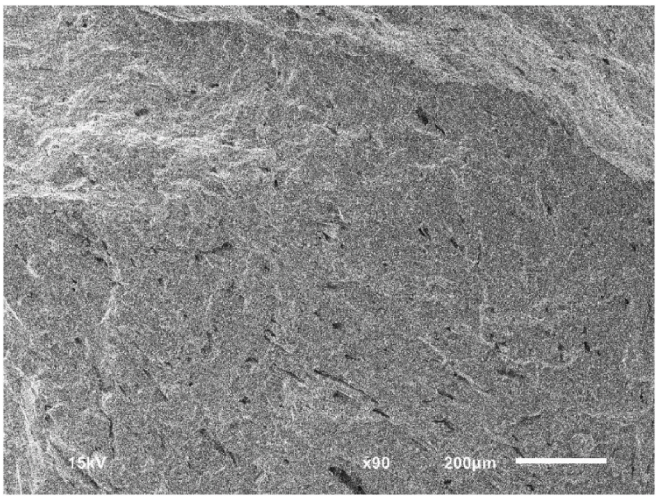

Fig. 4. Scanning electron microscopy micrograph of $BaLaCuS_3$ after thermal analysis.

dissolution, the mixture was heated and stirred periodically until the components were completely dissolved. The solutions of initial nitrates were formed by reactions:

$2BaCO_3 + La_2O_3 + 2Cu + 18HNO_3 \rightarrow 2Ba(NO_3)_2 + 2La(NO_3)_3 + 2CuNO_3 + 9H_2O + 4NO_2\uparrow + 2CO_2\uparrow$

The nitrate solution was then evaporated to a dry residue. The dry residue was transferred to a quartz beaker and heat treated at 900 °C degrees in the air. The result was a black color oxide mixture.

Sulfidation of the oxide mixture was carried out at 900 °C in a stream of sulfiding agents CS_2/H_2S and argon. The sulfiding agents are obtained by decomposition of NH_4CSN [11]. The reaction was being carried out for 5 h:

$2BaO + La_2O_3 + Cu_2O + 3CS_2 \rightarrow 2BaLaCuS_3 + 3CO_2$

The sulfiding gas stream was then percolated, but the argon stream was left to remove excess sulfur and to avoid subsequent condensation of the decomposition products of NH_4CSN. The quartz reactor was removed from the furnace and cooled to room temperature without blocking the argon stream. The final powder products of $BaLaCuS_3$ were yellow color. The following advantages of this synthesis route could be mentioned:

- Use of air-stable compounds with accurate stoichiometric composition.
- Greater homogeneity of the mixture after decomposition of the nitrate solution. This increases the yield of the product and reduces the production time.
- Faster process for the production of sulfide than the ampoule method. It took 5 h to use the oxide sulfidation method. For the ampoule synthesis method of the same compound, it took more than 48 h were taken [10].

3. Experimental

The simultaneous thermal analysis was performed in the He (99,999%, Russia) stream with the use of a Synchronous Thermal Analyzer STA 449 F3 Jupiter apparatus supplied with a (W3%Re – W25%Re) thermocouple. The evaluated powder sample weighed (90–100) ± 0.01 mg. The temperature adjustment accuracy was within 0.3 K. In the temperature range, where thermal effects were observed, the heating rate was 10 K/min. The data obtained from DSK/TG experiments were processed in the Proteus-6 software package [12]. The possible error in the melting enthalpy determination was ±18%.

The particle micromorphology was observed by SEM using an JSM-6510LV-EDS device. For SEM analysis, the powder sample was

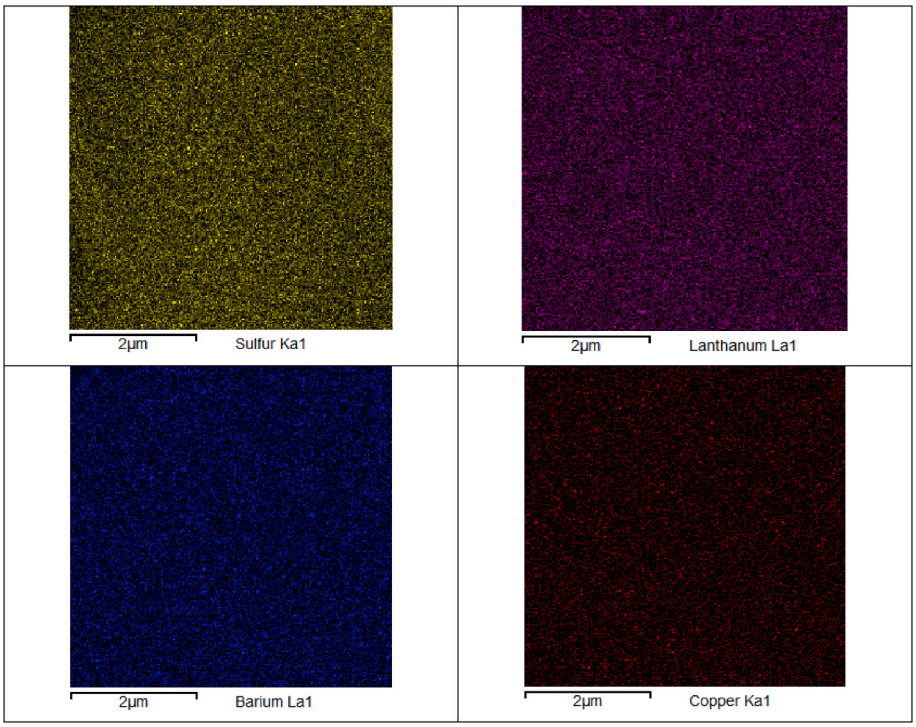

Fig. 5. Maps of atomic distribution of the edge area.

Table 1
Comparison of experimental and optimized lattice constants and fractional atomic coordinates of $BaLaCuS_3$ (optimized coordinated shown in parentheses).

a (Å)	*b* (Å)	*c* (Å)	
11.316	4.236	11.724	[9]
11.1949	4.15	11.5942	This work
x	*y*	*z*	
0.81672 (0.81754)	0.25 (0.25)	0.50661 (0.50880)	Ba
0.48904 (0.48590)	0.25 (0.25)	0.31890 (0.32010)	La
0.25375 (0.25486)	0.75 (0.75)	0.21001 (0.20881)	Cu
0.22497 (0.22385)	0.25 (0.25)	0.29667 (0.29424)	S(1)
0.38814 (0.38440)	0.25 (0.25)	0.55809 (0.55830)	S(2)
0.45044 (0.44863)	0.75 (0.75)	0.14883 (0.14802)	S(3)

transferred to an electrically conductive carbon adhesive tape. The adhesive tape was attached to a copper cylinder with a diameter of 1 cm and a height of 1.5 cm. The sample was filled on top and the residues were shaken to avoid non-sticking particles.

The Infrared (IR) absorption spectrum was recorded with a Fourier-transform spectrometer VERTEX 80v (Bruker Optik GMBH) in the spectral range from 50 to 600 cm^{-1} with spectral resolution 4 cm^{-1}. The spectrum was taken from a tablet sample shaped as about 0.38 mm thick tablet of 13 mm in diameter and a weight of 0.0339 g. The tablet was prepared as follows: 0.0035 g of $BaLaCuS_3$ was thoroughly ground with 0.0304 g of Mipelon PM-200 of Mitsui Chemicals Group (average particle size – 10 μm), next cold pressing 10 ton, stress removal and heating in a die mold 8 min, cooling the die mold in a flowing water. The Globar was used for light source, and it was equipped with a Mylar Multilayer beam splitter and RT-DTG FIR as a detector (Bruker Optik GMBH).

The unpolarized Raman spectrum of $BaLaCuS_3$ powder was measured at ambient temperature in a right-angle scattering geometry in a frequency range from 15 cm^{-1} to 320 cm^{-1} by using a triple-grating spectrometer Trivista 777 (Princeton Instruments, USA) and a 659.57 nm laser Flamenco (Cobolt, Sweden). The spectral resolution was ~1 cm^{-1}. The glass cuvette with $BaLaCuS_3$ powder was placed inside of the vacuum cryostat to reduce the air contribution to the spectrum.

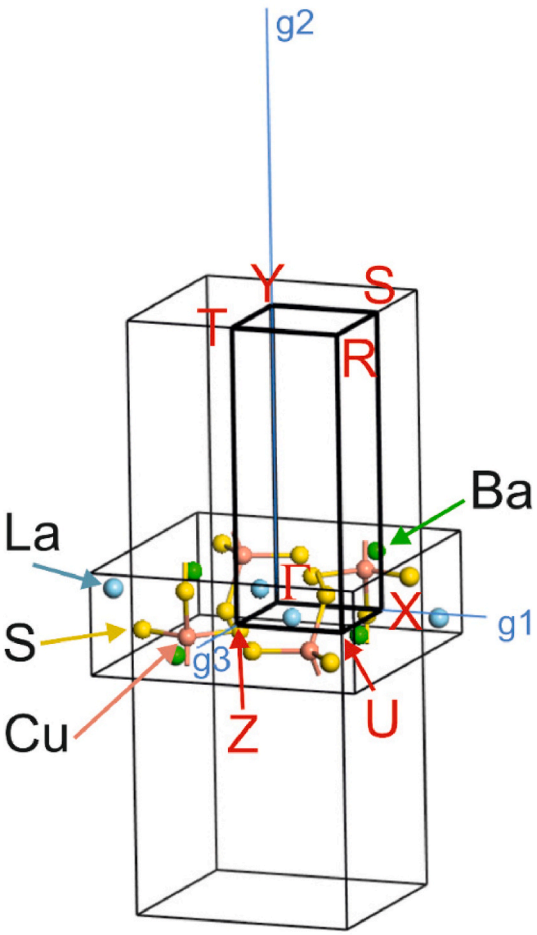

Fig. 6. Brillouin zone of the $BaLaCuS_3$.

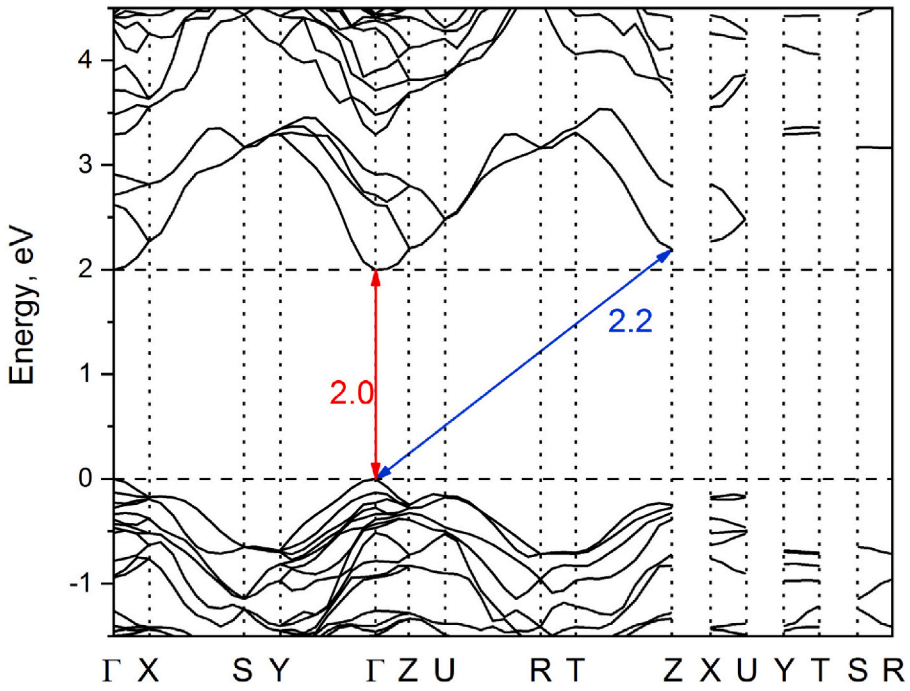

Fig. 7. Electronic band structure of $BaLaCuS_3$.

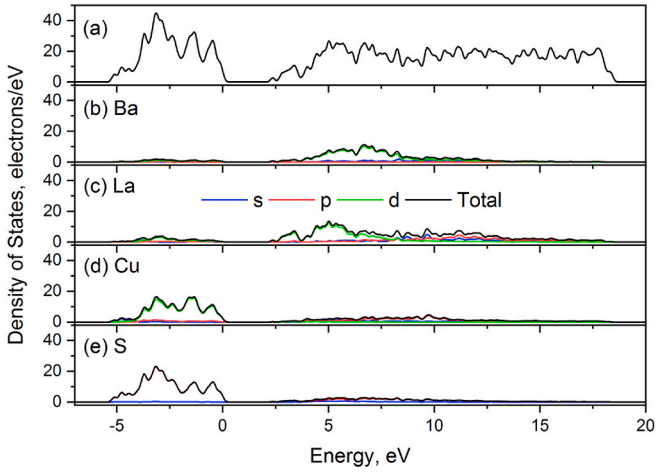

Fig. 8. Total (a) and partial density of states (b), (c), (d), (e) of $BaLaCuS_3$.

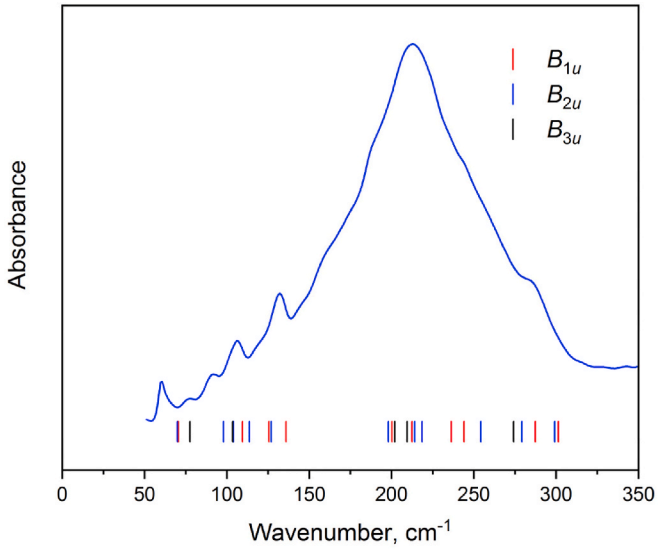

Fig. 9. Infrared spectrum of $BaLaCuS_3$ in Far-IR sub region. Vertical lines show the positions of calculated IR-active bands.

3.1. Calculation details

The first-principles density functional theory (DFT) calculations were carried out using the plane–wave pseudopotential approach (CASTEP package [13]). The lattice parameters and fractional atomic coordinates of $BaLaCuS_3$ were optimized under the LDA (local density approximation) that is based on the Perdew and Zunger [14] parameterization of the numerical results of Ceperley and Alder (CA-PZ) [15].

Norm conserving pseudopotentials generated on-the-fly in CASTEP code were used for calculation and include $5s^2$ $5p^6$ $6s^2$ electrons for Ba, $5s^2$ $5p^6$ $5d^1$ $6s^2$ electrons for La, $3d^{10}$ $4s^1$ electrons for Cu, and $3s^2$ $3p^4$ electrons for S as valence ones. The self-consistent field (SCF) tolerance was set to 5.0×10^{-8} eV/atom. The geometry optimization was performed with the convergence tolerance in maximal force and stress tensor set to 0.001 eVÅ^{-1} and 0.01 GPa correspondingly. The energy cutoff of 1210 eV was used with $2 \times 6 \times 2$ sampling of the Brillouin zone (BZ) using the Monkhorst–Pack scheme [16]. Calculations of the phonon spectra at the Gamma point of the BZ were performed using density functional perturbation theory (DFPT) and finite displacement method [17,18] based on the crystal system type.

4. Results and discussion

Fig. 1 show microstructure of $BaLaCuS_3$ powder prepared by sulphidation method. The particle size is irregular and in the range of 10–100 μm and particles have a disordered granular form.

In order to obtain the correct melting point and monitor the thermal effects, the compound melted twice. The first melting was done for the powder. To fix the number of thermal effects, the powder samples also begin to melt earlier than a single lump material. Also, after the first melting, the sample has a maximum area of contact with the crucible. The second melting of the substance gives precise temperatures and heat of effects and it is possible to estimate the maximum heating

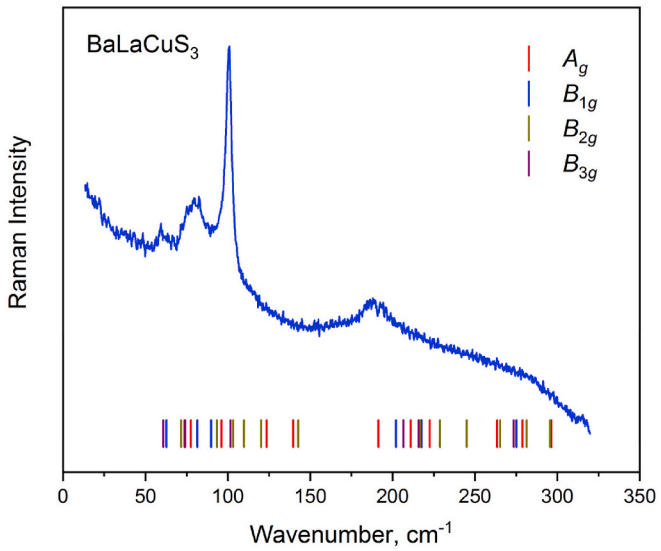

Fig. 10. Raman spectrum of $BaLaCuS_3$ powder recorded at 659.57 nm. Vertical lines show the positions of calculated Raman-active bands.

temperature to avoid overheating of the substance.

The $BaLaCuS_3$ powder was analyzed over the temperature range from 10 to 1400 °C (Fig. 2). The sample weight was 102 mg and the weight loss are not registered in the temperature cycling. The beginning of the endothermic effect is difficult to distinguish. Based on the intersection of the heating baseline and the DTA line, the effect start point is 1196.9 °C degrees. This effect is most likely due to the adhesion of small particles to larger ones. When heated, the fine particles melt on the side of touching the larger agglomerates and fuse with them, while also transferring excess energy to them. Since the process takes place at a constant increase in temperature, the adheision process proceeds all the time to a sharp melting point at 1259.7 °C degrees. The duration of the effect lasted for 62°. This longer duration is due to the large variation in particle size of the powder. The cooling curve shows a fluctuation of 1400 °C–1300 °C and the crystallization temperature is 1204.7 °C. Which means the sample was overheated and possibly bordered on the boiling effect.

Reheating of the $BaLaCuS_3$ after cooling to 50 °C degrees occurred to 1300 °C (Fig. 3). The endothermic effect related to substance melting $T_{melt} = 1258.9$ °C is observed on heating and the exothermic effect due to substance crystallization is detected at $T_{cryst} = 1259.6$ °C. The effect of overcooling for $BaLaCuS_3$ is not large and the difference between melting and crystallization points is 0.7 °C. The effect of overcooling is bound to congruous type of melting. Heat of melting determined for $BaLaCuS_3$ is $\Delta H_{melt} = 19.8$ kJ mol^{-1}.

At present, the thermal characteristics of $BaLaCuS_3$ are less studied. Temperature and thermal characteristics are known for $BaPrCuS_3$ T_{melt} = 1308 °C, ΔH_{melt} = 86.6 kJ mol^{-1} [19]. Only the melting point is known for $BaGdCuS_3$ T_{melt} = 1412 °C [20]. At the same time, it is possible to melt the $BaPrCuS_3$ incongruently, while it is obvious that the $BaLaCuS_3$ is melt congruently. Also, the heat of melting varies by 4 times. When compared to similar compounds, the heat of melting is comparable. Especially with compounds of a series of $EuLnCuS_3$ [19].

Fig. 4 show micrograph of the $BaLaCuS_3$ sample after thermal analysis. The sample was split. Morphology is fairly uniform but there are uniformly distributed pores of 1–2 μm in size. The atomic distribution is uniform and will satisfy the composition of the $BaLaCuS_3$ Fig. 5.

The structural parameters obtained by Ref. [9] were taken as initial for the *ab initio* geometry optimization included the unit cell parameters and atomic positions. The optimized structure is consistent with experimental data as shown in Table 1.

On the next step, the mechanical stability of $BaLaCuS_3$ lattice is

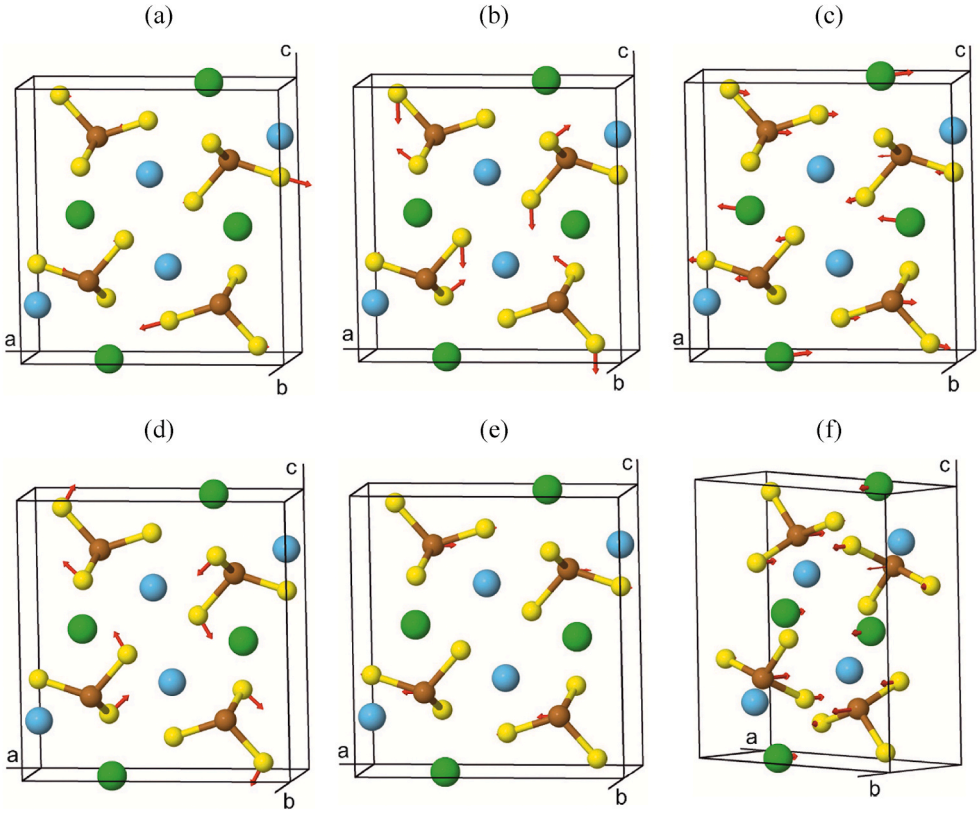

Fig. 11. Calculated atomic displacements in $BaLaCuS_3$ structure. (a) B_{1u} – 301.34 cm^{-1}, (b) B_{1u} – 287.28 cm^{-1}, (c) B_{1u} – 70.49 cm^{-1}, (d) A_{1g} – 191.35 cm^{-1}, (e) A_{1g} – 96.13 cm^{-1}, (f) B_{3g} – 60.80 cm^{-1}.

studied in terms of elastic constants and modulus [21,22]. Knowing the elastic behavior of the crystal lattice is based on the C_{ij} second order elastic constant matrix [23]. The calculated C_{ij} elastic matrix for $BaLaCuS_3$ (*Pnma* space group, orthorhombic symmetry) is given below. The elastic stability criteria (Born criteria) for crystal lattice with orthorhombic symmetry [23] should be written as $C_{11} > 0$, $C_{11}C_{22} > C_{12}^2$, $C_{11}C_{22}C_{33} + 2C_{12}C_{13}C_{23} - C_{11}C_{23}^2 - C_{22}C_{13}^2 - C_{33}C_{12}^2 > 0$, $C_{44} > 0$, $C_{55} > 0$, $C_{66} > 0$. The set of the above conditions is true for optimized structure of $BaLaCuS_3$ (Table 1) and we can say that structure $BaLaCuS_3$ is stable with respect to the mechanical properties. The calculated bulk modulus B at ambient conditions is 75.03 GPa. Obtained value is close to bulk modulus of germanium $B = 77.2$ GPa [24] and cubic zinc blende ZnS $B = 77$ GPa [25]. thus, hardness of this materials should be almost the same. Calculated B value is lower than in silicon (B = 98 GPa), while the band gap value (1.1 eV [9]) is almost twice large.

$$C_{ij=}\begin{pmatrix} 126.60 & 42.15 & 55.39 & & & \\ 42.15 & 126.33 & 57.32 & & & \\ 55.39 & 57.32 & 112.58 & & & \\ & & & 48.34 & & \\ & & & & 43.77 & \\ & & & & & 38.04 \end{pmatrix} \quad (1)$$

The path along BZ high-symmetry points was chosen as Γ–X–S–Y–Γ–Z–U–R–T–Z|X–U|Y–T|S–R for the $BaLaCuS_3$ electronic band structure calculations. Coordinates of these points are: Γ(0, 0, 0), R(0.5, 0.5, 0.5), S(0.5, 0.5, 0), T(0, 0.5, 0.5), U(0.5, 0, 0.5), X(0.5, 0, 0), Y(0, 0.5, 0), Z(0, 0.5, 0.5) and the path is depicted in Fig. 6. Calculated electronic band structure of $BaLaCuS_3$ is presented in Fig. 7.

The band gap value is defined as the distance between the minimum of conduction band (MCB) and the maximum of valence band (MVB). It is clearly seen from Fig. 7 that MCB is well localized in Γ-point and the MVB is located at the center of Brillouin zone too. The obtained value of band gap for direct electronic transitions (E^d_g) calculated using LDA approximation is equal 0.779 eV. Obtained value is less than obtained from experiment ($E_g = 2.0$ eV) [10] due to the fact that DFT calculations in local density approximation underestimates the experimental value and this situation is common for the density functional theory because of the presence of well-known band gap underestimation problem. As noted earlier [26], the DFT effective potential is determined only with an additive constant that depend on the total set of electrons in the system. The well-known procedure of artificially increasing the band gap value (scissor operator) was used and all conduction bands shifted up to 2.0 eV. Thus, we can conclude that $BaLaCuS_3$ is a typical direct gap semiconductor with transition point being the center of the Brillouin zone. The difference between direct and indirect electronic transitions equal to 0.2 eV (see Fig. 7).

The total and partial density of states of the $BaLaCuS_3$ structure are plotted in Fig. 8. As a result of the figure analysis, one can find that the maximum of valence band is formed by d-electrons of copper and p-electrons of sulfur, thus, the MVB is formed by electrons of CuS_4 tetrahedra. The MCB is constructed mostly by d-electrons of lanthanum ions. It is clearly seen, that the contribution of the barium ions to the MVB and MCB significantly less than other ions, thus we can conclude that semiconducting behaviors of $BaLaCuS_3$ connected with CuS_4 tetrahedra and La ions.

The Infrared анв Raman spectra from $BaLaCuS_3$ powder are shown in Figs. 9 and 10 correspondingly. The mechanical representation for the $BaLaCuS_3$ at the Brillouin zone center is $\Gamma_{vibr} = 12A_g + 6A_u + 6B_{1g} + 12B_{1u} + 12B_{2g} + 6B_{2u} + 6B_{3g} + 12B_{3u}$ where Infrared active modes are $\Gamma_{Infrared} = 11B_{1u} + 5B_{2u} + 11B_{3u}$ (acoustic modes not included) and Raman active modes are $\Gamma_{Raman} = 12A_g + 6B_{1g} + 12B_{2g} + 6B_{3g}$. The acoustic modes are $\Gamma_{Acoustic} = B_{1u} + B_{2u} + B_{3u}$. The A_u modes are silent. The calculated phonon frequencies of the $BaLaCuS_3$ are presented in Table S2 of Supporting information and plotted by vertical lines given in Figs. 9 and 10. The according to the lattice dynamics simulation, we can conclude that spectral bands above 195 cm^{-1} in Fig. 9 related to CuS_4 vibrational modes. It is interesting that difference between frequencies of Cu–S stretching and CuS_4 bending-like vibrations is small, for example, see Fig. 11 (a) and (b). The strongest band at 212 cm^{-1} in Fig. 9 is related to rotation of CuS_4 tetrahedra. Bands in the range of 80–140 cm^{-1} are associated with translations of copper, barium and lanthanum ions. The band below 80 cm^{-1} are related to displacement of structural layers as shown, for example, in Fig. 11 (c). Spectral bands above 180 cm^{-1} in Raman spectrum (Fig. 10) are vibrations of CuS_4. The weak band at 188 cm^{-1} is associated with rotations of CuS_4 as shown in Fig. 11 (d). Band from 65 to 150 cm^{-1} in Raman spectrum are translational vibrations. The strongest line at 100 cm^{-1} is a translation of copper atoms, see Fig. 11 (e). Broad band at 80 cm^{-1} corresponds to translational vibrations of CuS_4, Ba and La, as well as combinations of such translations. The lowest Raman band is attributed to layers vibrations (Fig. 11 (f)).

5. Conclusions

This study addresses the relative fast synthesis of $BaLaCuS_3$ powder and it's thermal, electronic, elastic and vibrational properties. The time of synthesis of $BaLaCuS_3$ by the proposed method is almost ten times smaller than the ampoule synthesis method. The melting point is found to be around 1259 °C. According to the calculation of electronic band structure, the $BaLaCuS_3$ is a direct band gap semiconductor and semiconducting behaviors of $BaLaCuS_3$ connected with CuS_4 tetrahedra and La ions. The theoretical calculations of vibration spectra are in agreement with experiment and vibrations of $BaLaCuS_3$ structural units discussed for the first time.

CRediT authorship contribution statement

A.S. Oreshonkov: Conceptualization, Formal analysis, Writing - original draft, Supervision, Project administration. **N.O. Azarapin:** Formal analysis, Investigation, Resources. **N.P. Shestakov:** Formal analysis, Investigation. **S.V. Adichtchev:** Formal analysis, Investigation.

Declaration of competing interest

The authors declare that they have no known competing financial interests or personal relationships that could have appeared to influence the work reported in this paper.

Acknowledgements

The reported study was funded by RFBR, project numbers: 18-03-00750, 18-05-00682 and 18-32-20011. The authors would like to thank Alexey A. Lubin for his studies on SEM. The studies were carried out on the basis of a laboratory of electron and probe microscopy in REC 'Nanotechnologies'. We are grateful to the Krasnoyarsk Regional Center of Research Equipment of Federal Research Center « Krasnoyarsk Science Center SB RAS » for the provided Bruker Vertex 80v. The experimental part corresponding to Raman measurements was supported by the Ministry of Education and Science of the Russian Federation, grant no AAAA-A17-117052410033-9.

Appendix A. Supplementary data

Supplementary data to this article can be found online at https://doi.org/10.1016/j.jpcs.2020.109670.

References

[1] V.S. Vavilov, Phys. Usp. 37 (3) (1994) 269–277, https://doi.org/10.1070/PU1994v037n03ABEH000012.

[2] Technical report Oak Ridge National Laboratory, Wide bandgap semiconductor opportunities in power electronics, https://www.osti.gov/biblio/1415915/2017 (Publication date: 2018.01.01).
[3] Ü. Özgür, YaI. Alivov, C. Liu, A. Teke, M.A. Reshchikov, S. Doğan, V. Avrutin, S.-J. Cho, H. Morkoç, J. Appl. Phys. 98 (4) (2005), 041301, https://doi.org/10.1063/1.1992666.
[4] M. Pelaez, N.T. Nolan, S.C. Pillai, M.K. Seery, P. Falaras, A.G. Kontos, P.S. M. Dunlop, J.W.J. Hamilton, J.A. Byrne, K. O'Shea, M.H. Entezari, D.D. Dionysiou, Appl. Catal. B Environ. 125 (2012) 331–349, https://doi.org/10.1016/j.apcatb.2012.05.036.
[5] A. Fujishima, K. Honda, Nature 238 (1972) 37–38, https://doi.org/10.1038/238037a0.
[6] J.A. Rohr, J. Lipton, J. Kong, S.A. Maclean, A.D. Taylor, Joule 4 (4) (2020) 1–10, https://doi.org/10.1016/j.joule.2020.02.005.
[7] W. Shockley, H.J. Queisser, J. Appl. Phys. 32 (1961) 510–519, https://doi.org/10.1063/1.1736034.
[8] S. Rühle, Sol. Energy 130 (2016) 139–147, https://doi.org/10.1016/j.solener.2016.02.015.
[9] A.S. Oreshonkov, E.M. Roginskii, V.V. Atuchin, J. Phys. Chem. Solid. 137 (2020) 109219, https://doi.org/10.1016/j.jpcs.2019.109219.
[10] A.E. Christuk, P. Wu, J.A. Ibers, J. Solid State Chem. 110 (1994) 330–336, https://doi.org/10.1006/jssc.1994.1176.
[11] M. Ohta, S. Hirai, H. Kato, V.V. Sokolov, V.V. Bakovets, Mater. Trans. 50 (7) (2009) 1885–1889, https://doi.org/10.2320/matertrans.M2009060.
[12] NETZSCH Proteus 6, Thermic Analyses – User's and Software Manuals, 2012. Germany.
[13] S.J. Clark, M.D. Segall, C.J. Pickard, P.J. Hasnip, M.J. Probert, K. Refson, M. C. Payne, Z. Kristallogr. 220 (5–6) (2005) 567–570, https://doi.org/10.1524/zkri.220.5.567.65075.
[14] J.P. Perdew, A. Zunger, Phys. Rev. B 23 (1981) 5048–5079.
[15] D.M. Ceperley, D.J. Alder, Phys. Rev. Lett. 45 (1980) 566–569, https://doi.org/10.1103/PhysRevLett.45.566.
[16] H.J. Monkhorst, J.D. Pack, Phys. Rev. B 13 (1976) 5188–5192, https://doi.org/10.1103/PhysRevB.13.5188.
[17] D. Porezag, M.R. Pederson, Phys. Rev. B 54 (1996) 7830–7836, https://doi.org/10.1103/PhysRevB.54.7830.
[18] K. Refson, P.R. Tulip, S.J. Clark, Phys. Rev. B 73 (2006) 155114, https://doi.org/10.1103/PhysRevB.73.155114.
[19] N.O. Azarapin, A.S. Aleksandrovsky, V.V. Atuchin, T.A. Gavrilova, A.S. Krylov, M. S. Molokeev, S. Mukherjee, A.S. Oreshonkov, O.V. Andreev, J. Alloys Compd. 832 (2020) 153134, https://doi.org/10.1016/j.jallcom.2019.153134.
[20] N.V. Sikerina, A.V. Solov'eva, E.N. Toroshchin, O.V. Andreev, Russ. J. Inorg. Chem. 52 (12) (2007) 1982–1986, https://doi.org/10.1134/S0036023607120285.
[21] M. Born, I. Math. Proc. Cambridge 36 (2) (1940) 160–172.
[22] M. Born, K. Huang, Dynamics Theory of Crystal Lattices, Oxford University Press, UK, 1954. Oxford.
[23] F. Mouhat, F.-X. Coudert, Phys. Rev. B 90 (22) (2014) 224104, https://doi.org/10.1103/PhysRevB.90.224104.
[24] G. Misra, P. Tripathi, S.C. Goyal, Phil. Mag. Lett. 87 (6) (2007) 393–401, https://doi.org/10.1080/09500830701203131.
[25] M.L. Cohen, Phys. Rev. B 32 (12–15) (1985) 7988–7991, https://doi.org/10.1103/PhysRevB.32.7988.
[26] J.P. Perdew, Int. J. Quant. Chem. 28 (S19) (1985) 497–523, https://doi.org/10.1002/qua.560280846.